



# A fully dynamic multi-compartmental poroelastic system: Application to aqueductal stenosis



Dean Chou<sup>a</sup>, John C. Vardakis<sup>b</sup>, Liwei Guo<sup>b</sup>, Brett J. Tully<sup>c</sup>, Yiannis Ventikos<sup>b,\*</sup>

<sup>a</sup> Institute of Biomedical Engineering & Department of Engineering Science, University of Oxford, Oxford OX1 3PJ, UK

<sup>b</sup> Department of Mechanical Engineering, University College London, Torrington Place, London WC1E 7JE, UK

<sup>c</sup> First Light Fusion Ltd., Begbroke Science Park, Begbroke, Oxfordshire, OX5 1PF, UK

## ARTICLE INFO

### Article history:

Accepted 21 November 2015

### Keywords:

Multiple-network poroelastic theory  
Hydrocephalus  
Aqueduct  
Cerebrospinal fluid  
Stenosis

## ABSTRACT

This study proposes the implementation of a fully dynamic four-network poroelastic model which is underpinned by multiple-network poroelastic theory (MPET), in order to account for the effects of varying stages of aqueductal stenosis and atresia during acute hydrocephalus. The innovation of the fully dynamic MPET implementation is that it avoids the commonplace assumption of quasi-steady behaviour; instead, it incorporates all transient terms in the casting of the equations and in the numerical solution of the resulting discrete system.

It was observed that the application of mild stenosis allows for a constant value of amalgamated ventricular displacement in under 2.4 h, whereas the application of a severe stenosis delays this settlement to approximately 10 h. A completely blocked aqueduct does not show a clear sign of reaching a steady ventricular displacement after 24 h. The increasing ventricular pressure (complemented with ventriculomegaly) during severe stenosis is causing the trans-parenchymal tissue region to respond, and this coping mechanism is most attenuated at the regions closest to the skull and the ventricles. After 9 h, the parenchymal tissue shows to be coping well with the additional pressure burden, since both ventriculomegaly and ventricular CSF (cerebrospinal fluid) pressure show small increases between 9 and 24 h. Localised swelling in the periventricular region could also be observed through CSF fluid content, whilst dilation results showed stretch and compression of cortical tissue adjacent to the ventricles and skull.

© 2015 The Authors. Published by Elsevier Ltd. This is an open access article under the CC BY-NC-ND license (<http://creativecommons.org/licenses/by-nc-nd/4.0/>).

## 1. Introduction

### 1.1. Hydrocephalus

Hydrocephalus can be described as the abnormal accumulation of Cerebrospinal fluid (CSF) within the brain (Tully and Ventikos, 2011; Rekate, 2009; Thompson, 2009; Stagno et al., 2013). Hydrocephalus is classified as obstructive when the point of CSF blockage or distinct lesion lies within the ventricular system and hinders flow before it enters the subarachnoid space (Corns and Martin, 2012). If this is not the case, it is generally known as communicating hydrocephalus.

### 1.2. Aqueductal stenosis

Cinalli et al. (2010) describe the aqueduct as a curved conduit around 15 mm in length and up to 3 mm in width, with concavity

towards the base of the skull and a highly variable cross section, where there is a shape transition from triangular (cranial orifice), oval in the central area and finally resembles an inverted “U” at the level of the inferior colliculi (Jellinger, 1986). The interior lumen of the Sylvian aqueduct is lined with ependymal cells (Bruni, 1998). This cell layer however, is not confined to being unicellular, and in some cases ependymal cells may even be absent from the lining of the aqueduct. These denuded areas pose a problem since they may lead to the bridging of the canal via an overproduction of glial fibrils.

Mass lesions (from tumours or vascular malformations) may aid in the stenosis/atresia of the aqueduct of Sylvius. In addition, histopathological classifications of “nontumoral aqueduct anomalies” have been confirmed as *Stenosis*, *Forking*, *Septum formation* and *Gliotic stenosis* (Cinalli, 2010; Russel, 1949; Spennato et al., 2013). During stenosis, the aqueduct is forced to narrow and the ependymal lining of the lumen remains intact. Gliotic stenosis may be considered an acquired condition and is characterised by the occlusion of the aqueduct due to an overproduction of glial fibres or the creation of multiple channels that lack an evident ependymal lining (Cinalli, 2010).

\* Corresponding author. Tel.: +44 20 7679 7068/3908.

E-mail address: [y.ventikos@ucl.ac.uk](mailto:y.ventikos@ucl.ac.uk) (Y. Ventikos).

### 1.3. Modelling aqueductal stenosis using poroelasticity

There are numerous works in the literature that have utilised a poroelastic approach in modelling parenchymal tissue (Kaczmarek et al., 1997; Levine, 1999, 2000; Smillie et al., 2005; Shahim et al., 2012; Tully and Ventikos, 2009, 2011; Vardakis et al., 2013a). Considering aqueductal stenosis or atresia whilst modelling the brain as a poroelastic medium in the manner outlined in this work (excluding any CFD coupling) yields a narrower selection of relevant work (Smillie et al., 2005; Sobey and Wirth, 2006).

In this manuscript, we investigate the effect of artificially imposed aqueductal stenosis and atresia using a novel application of a one dimensional, fully dynamic multiple-network poroelastic (MPET) formulation. The MPET formulation allows the tracking of the parenchymal matrix displacement (relative to a reference position), which assimilates the pore pressures of the respective fluid networks. Once the methodology has been described, some results based on aqueductal stenosis follow, along with the interpretation of these results.

## 2. Methods

In this section, we outline the definition of the MPET framework that is used to model parenchymal tissue, along with its adaptation to the cerebral environment. We then proceed with outlining the spherical representation of the cerebral environment that dictates the nature of the 1D MPET model. Boundary conditions are then discussed, along with justification of the poroelastic constants.

### 2.1. Multiple-network poroelastic formulation

The classical form of Biot's consolidation model (Biot, 1941) is described for an isotropic and incompressible solid matrix and homogenous porous medium. For a simple poroelastic medium to be defined, an equilibrium equation is needed to define elastic deformation and Darcy's law is used to model fluid flow. Finally, mass conservation is also required. Biologically, the quadruple MPET system is derived by accommodating a high pressure arterial network (a), lower pressure arteriole/capillary network (c), interstitial fluid (ISF)/CSF network (e) and finally a venous network (v) (Tully and Ventikos, 2011). One may cast equations to be solved for the mean displacement of particles forming the solid matrix,  $\mathbf{u}$ , and the scalar pore pressures of the extended multicompartmental porous medium ( $p^a$ ,  $p^c$ ,  $p^e$ ,  $p^v$ ) which is defined through multiple-network poroelastic theory (MPET). A general MPET derivation will now follow.

The stress-strain relationship for a solid is re-written in the form reminiscent of Rice and Cleary (1976), which makes use of Lamé's constants ( $G$ ,  $\lambda$ ), and subsequently extended to multiple-porosity poroelasticity:

$$\sigma_{ij} = 2G\epsilon_{ij} + \lambda\epsilon_{kk}\delta_{ij} - \sum_{A=a,e,c,v} \alpha^A p^A \delta_{ij} \quad (1)$$

In the above equation, the Biot-Willis coefficient  $\alpha$  can be interpreted from both a microscopic and macroscopic perspective. The global version of the Biot-Willis parameter allows for Eq. (1) to be interpreted as the weighted average contribution of each fluid network to the constitutive effective stress of the multiple-network system. The range of values for the global Biot-Willis coefficient is  $\alpha[0, 1]$ .

Darcy's Law is extended to take into account all of the fluid networks, hence:

$$\mathbf{q}_A = -\frac{k_A}{\mu_A} (\nabla p^A), \quad A = a, e, c, v \quad (2)$$

The first governing equation of motion for a unit volume within the MPET framework is given by:

$$\sigma_{ij,j} + \left[ \sum_{A=a,e,c,v} n^A (\rho^A - \rho_s) + \rho_s \right] (b_i - \ddot{u}_i) - \sum_{A=a,e,c,v} \rho^A (\dot{w}_i^A + w_j^A w_{ij}^A) = 0 \quad (3)$$

$\sigma_{ij,j}$  is the stress within the solid matrix. The convention will be made to align a positive value of this stress with a tension.  $u_i$  describes the mean displacement of elements forming the solid matrix,  $w_i$  is the ratio of fluid flow to cross sectional area and  $\sum_{a=1}^A n^a \rho^a + (1-n)\rho_s$  is the total density of the system,  $\rho_s$  is the solid density and  $\sum_{a=1}^A n^a$  is the total porosity of all the individual fluid networks. Finally,  $b_i$  is the body force per unit mass.

The second governing equation of motion is that defining the momentum of each individual fluid network:

$$p_i^A - R_i^A - \rho^A (b_i - \ddot{u}_i) - \frac{\rho^A}{n^A} (\dot{w}_i^A + w_j^A w_{ij}^A) = 0 \quad (4)$$

In the above,  $R_i^A$  is the viscous drag force utilising Darcy's seepage law (Zienkiewicz et al., 1999).

Flow conservation for the fluid phase is given by:

$$S_e^A \dot{p}^A + \alpha^A \dot{\epsilon}_{ii} + w_{i,i}^A + \frac{1}{\rho^A} \dot{p}^A = \sum_{A=a,e,c,v} \overbrace{\omega_{ij}}^{\dot{s}_{ij}} (p_j - p_i) \quad (5)$$

$\dot{\epsilon}_{ii}$  is the rate of change of the strain within the solid matrix,  $\alpha^A$  is the Biot parameter of the fluid network in question and finally the right hand side possesses either source ( $\dot{s}_{ij} > 0$ ) or sink ( $\dot{s}_{ij} < 0$ ) densities and  $\mathbf{q}$  represents the fluid flux vector. From Eq. (5), the fluid phase continuity equations include the sum of all compartmental fluxes ( $\dot{s}_{ij}$ ), from network  $j$  to  $i$ . Here, the transfer is considered to be driven by a hydrostatic pressure gradient, whilst  $\omega_{ij}$  is the transfer coefficient scaling the flow from network  $j$  to network  $i$ .

Eliminating  $w_i^A$  from Eq. (4) as in Tully and Ventikos (2011), one may then focus on the primary variables  $\mathbf{u}$  and  $p$ . Utilising Darcy's seepage law (Zienkiewicz et al., 1999) and Eq. (4), one obtains:

$$w_i^A = k_{ij}^A p_i^A - k_{ij}^A \rho^A (b_j - \ddot{u}_j) \quad (6)$$

$k_{ij}^A$  defines the anisotropic permeability coefficient. If isotropy is sought, this value is replaced by a single  $k^A$  constant (which is assumed in this manuscript). Substituting Eq. (6) to into Eq. (5), one obtains:

$$S_e^A \dot{p}^A + \alpha^A \dot{\epsilon}_{ii} + \left[ k_{ij}^A p_i^A - k_{ij}^A \rho^A (b_j - \ddot{u}_j) \right] - \sum_{A=a,e,c,v} \dot{s}_{ij} = 0 \quad (7)$$

Finally, Eq. (1) is combined with Eq. (3), and ignoring the fluid acceleration relative to the solid and the convective terms of this acceleration, one obtains the final system:

$$\begin{aligned} \nabla \cdot \boldsymbol{\sigma} - \sum_{A=a,e,c,v} \alpha^A \nabla p^A + \rho_s (\mathbf{b} - \ddot{\mathbf{u}}) &= 0 \\ S_e^A \dot{p}^A + \alpha^A \dot{\epsilon} + \nabla \cdot \left[ k^A \cdot \rho^A (\mathbf{b} - \ddot{\mathbf{u}}) - k^A \cdot \nabla p^A \right] - \sum_{A=a,e,c,v} \dot{s}_{ij} &= 0 \end{aligned} \quad (8a-b)$$

### 2.2. Adaptation to the cerebral environment

The first stage of adapting an MPET modelling framework to describe the transfer of fluid through the brain parenchyma, is to postulate the overall formation of the MPET network. In this work, the solid porous matrix represents the tissue in the brain parenchyma, whilst the communicating fluid phases that will be taken into account are: arterial blood (a), arteriole/capillary blood (c), venous blood (v) and the CSF/ISF (e) space, i.e. four networks (Tully and Ventikos, 2011). Representing the  $\sum \omega_{ij}(p^j - p^i)$  terms on the right hand side of Eq. (4) as  $\dot{s}_{ij}$ , the field Eqs. (5) and (6) for the four compartment MPET model are as follows:

$$\begin{aligned} \left[ G \nabla^2 \mathbf{u} + \left( \frac{G}{1-2\nu} \right) \nabla (\nabla \cdot \mathbf{u}) - \alpha^a \nabla p^a - \alpha^c \nabla p^c - \alpha^e \nabla p^e - \alpha^v \nabla p^v \right] &= \rho^s \frac{\partial^2 \mathbf{u}}{\partial t^2} \\ \frac{\partial}{\partial t} (S_e^a p^a + \alpha^a \nabla \cdot \mathbf{u}) - \left[ \frac{k_a}{\mu_a} \nabla^2 p^a + |\dot{s}_{a-c}| \right] &= \frac{k_a \rho^a}{\mu_a} \frac{\partial^2}{\partial t^2} (\nabla \cdot \mathbf{u}) \\ \frac{\partial}{\partial t} (S_e^c p^c + \alpha^c \nabla \cdot \mathbf{u}) - \left[ \frac{k_c}{\mu_c} \nabla^2 p^c - |\dot{s}_{a-c}| + |\dot{s}_{c-e}| + |\dot{s}_{c-v}| \right] &= \frac{k_c \rho^c}{\mu_c} \frac{\partial^2}{\partial t^2} (\nabla \cdot \mathbf{u}) \\ \frac{\partial}{\partial t} (S_e^e p^e + \alpha^e \nabla \cdot \mathbf{u}) - \left[ \frac{k_e}{\mu_e} \nabla^2 p^e - |\dot{s}_{c-e}| + |\dot{s}_{e-v}| \right] &= \frac{k_e \rho^e}{\mu_e} \frac{\partial^2}{\partial t^2} (\nabla \cdot \mathbf{u}) \\ \frac{\partial}{\partial t} (S_e^v p^v + \alpha^v \nabla \cdot \mathbf{u}) - \left[ \frac{k_v}{\mu_v} \nabla^2 p^v - |\dot{s}_{c-v}| - |\dot{s}_{e-v}| \right] &= \frac{k_v \rho^v}{\mu_v} \frac{\partial^2}{\partial t^2} (\nabla \cdot \mathbf{u}) \end{aligned} \quad (9a-e)$$

In the above equation, the  $S_e$  term is the inverse of the specific storage (a measure of the released fluid volume per unit pressure in the control volume) at constant strain for each fluid compartment.

The transfer of fluid between four fluid networks is required to obey the law of continuity for the entire system, and so directionality between fluid compartments must be accurately specified. Fig. 1a provides a summary of the directional fluid restrictions placed. It is noted that the current MPET template takes into account the physiological relationship between CSF and ISF best represented in the recent literature (Iliff et al., 2012). It has been shown that CSF and ISF are in continuous exchange. The convective influx of CSF along the periarterial space facilitates this process. The *glymphatic system* recently discovered best portrays this macroscopic process, which also takes into account strategically located Aquaporin-4 channels. In previous work by the same authors (Vardakis et al., 2013b), this aquaporin channel was taken into account by a very simple functional relationship which varied the base permeability of the CSF compartment in the MPET system. In this work, the permeability of the CSF/ISF compartment keeps a constant value (see Table 1). The latter four equations are applied to the pressure gradients of the deformed brain configuration, whereas the stress equilibrium Eq. (9a) combines

the pressure derivatives from the undeformed configuration. This adaptation is driven by the overall need to visualise the displacements obtained from the deformed brain configuration under the auspice of small-strain linear elasticity.

### 2.3. Geometry

In Fig. 1b, the spherical representation of the cerebral environment that dictates the nature of the 1D MPET model is shown. The poroelastic parenchymal tissue is modelled between two concentric shells representing the skull (incorporating the scalp and dura) and ependyma of the ventricles, with respective radii of  $r_M$  and  $r_v$ . There is no distinction between white and grey matter within this parenchymal region.

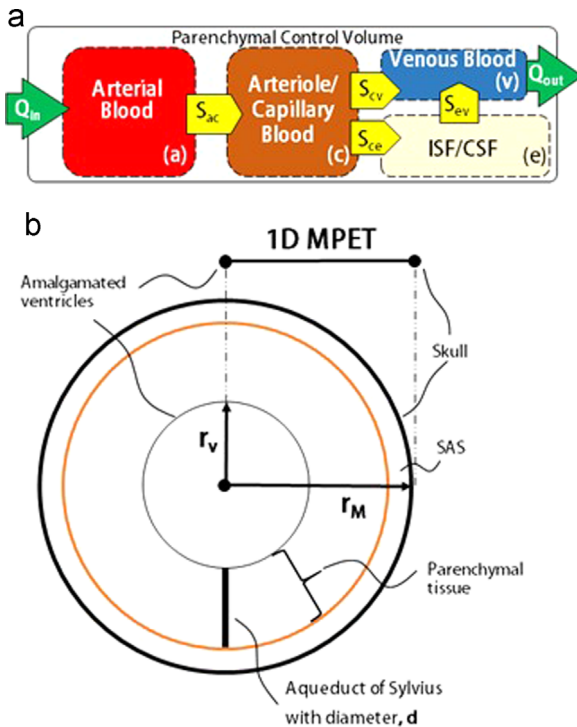


**Fig. 1.** The fluid transfer restrictions placed between the four compartments and the representative spherical representation of the 1D MPET model. (a) It can be seen that flow is prohibited between the CSF and arterial network, whilst directional transfer exists between  $a$  and  $c$ ,  $c$  and  $v$ ,  $c$  and  $e$  and finally  $e$  and  $v$ . (b) The parenchymal tissue of the brain is simplified to a spherical shell. The lumped representation of the cerebral ventricles is connected to the SAS via an idealised representation of the aqueduct of Sylvius.

**Table 1**

List of the parameter values used in the MPET framework.

Parameter	Value	[Units]	Parameter	Value	[Units]
$r_v$	3	cm	$\omega_{ac}$	$1.5 \times 10^{-19}$	$\text{m}^2 \text{N}^{-1} \text{s}^{-1}$
$r_M$	10	cm	$\omega_{cv}$	$1.5 \times 10^{-19}$	$\text{m}^2 \text{N}^{-1} \text{s}^{-1}$
$L$	7	cm	$\omega_{ev}$	$1.0 \times 10^{-13}$	$\text{m}^2 \text{N}^{-1} \text{s}^{-1}$
$d$	4, 1, 0.25 and 0	mm	$\omega_{ce}$	$2.0 \times 10^{-19}$	$\text{m}^2 \text{N}^{-1} \text{s}^{-1}$
$E$	584	$\text{N m}^{-2}$	$k_{a,c,v}$	$1.0 \times 10^{-10}$	$\text{m}^2$
$p_{bp}$	650	$\text{N m}^{-2}$	$k_e$	$1.4 \times 10^{-14}$	$\text{m}^2$
$p_{bpA}$	$13.3 \times 10^3$	$\text{N m}^{-2}$	$K$	649	$\text{N m}^{-2}$
$R$	$8.5 \times 10^{13}$	$\text{m}^{-3}$	$\lambda$	505	$\text{N m}^{-2}$
$Q_p, Q_o$	$5.8 \times 10^{-9}$	$\text{m}^3 \text{s}^{-1}$	$G$	216	$\text{N m}^{-2}$
$\kappa_{c \rightarrow vent}$	$6.4 \times 10^{-4}$	$\text{m}^5 \text{s kg}^{-1}$	$\alpha^{a,e,c,v}$	0.9955	
$\mu_e$	$8.9 \times 10^{-4}$	$\text{N s m}^{-2}$	$\nu$	0.35	
$\mu_{a,c,v}$	$2.67 \times 10^{-3}$	$\text{N s m}^{-2}$	$B$	0.99	
$\rho^e$	1007	$\text{kg m}^{-3}$	$S_e^{a,e,c,v}$	$4.47 \times 10^{-7}$	$\text{m}^2 \text{N}^{-1}$
$\rho^{a,c,v}$	1060	$\text{kg m}^{-3}$			
$\rho^s$	1038	$\text{kg m}^{-3}$			

### 2.4. Boundary conditions and time integration

The MPET system is completed with boundary conditions for each of the four compartments ( $a, e, c, v$ ), in which  $\Gamma_s$  and  $\Gamma_v$  are boundary conditions at the skull and ventricles respectively. The skull is assumed rigid, since the model is assumed to apply for adult cases, hence:

$$\mathbf{u} = \mathbf{0} \quad \text{on } \Gamma_s \quad (10)$$

For continuity of stresses, the poroelastic stress present in the brain's tissue must balance the ventricular pressure exerted by the CSF within the inner ventricular wall, hence:

$$-p^v \mathbf{n} = \sigma_{ij} \cdot \mathbf{n} \quad \text{on } \Gamma_v \quad (11)$$

CSF secretion is assumed to take place in the cerebral ventricles, and is of the order of  $Q_p \approx 500 \text{ ml/day}$  or  $5.8 \times 10^{-9} \text{ m}^3 \text{ s}^{-1}$ . In the case of an open, idealised cylindrical aqueduct, the steady Hagen–Poiseuille relationship for the flow rate is given by:

$$Q_{HP} = \frac{\pi d^4}{128 \mu_e L} (p_v - p_s) \quad (12)$$

In the above equation,  $p_v$  and  $p_s$  denote the ventricular and subarachnoid pressures, whilst  $L$  denotes the radial distance between ventricles and skull. The diameter  $d$  is that of the cerebral aqueduct(s) (subsequently stenosed and blocked), and is given in Table 1. We should note that this assumption by no means restricts the generality of the model, since, as it has been shown, it is straightforward to incorporate non-idealised, anatomically accurate aqueduct configurations and couple detailed hydrodynamics to the MPET model (Vardakis et al., 2013a).

Conservation of mass of fluid within the ventricular system involves the amount of CSF produced by the choroid plexuses, ventricular change of volume and outflow, as necessary:

$$Q_p = Q_{HP} - 4\pi k^e (r_1 + u_1^n) \frac{\partial}{\partial r} (p^e(r, t)) + 4\pi (r_1 + u_1^n)^2 \frac{\partial}{\partial t} (u(r, t)) \quad (13)$$

Aqueduct stenosis and atresia is enforced by altering the diameter of the aqueduct (see Eqs. (12) and (13)) for the values: 4 mm, 1 mm, 0.25 mm and 0 mm (shown in Table 1) respectively. These diameters are attributed to a patent (open) aqueduct, mild stenosis, severe stenosis and completely blocked aqueduct respectively.

CSF being produced from the blood results in a pressure drop in the arteriole/capillary blood network:

$$\frac{\partial}{\partial r} (p_c) = \frac{Q_p}{\kappa_{c \rightarrow vent}} \quad \text{on } \Gamma_v \quad (14)$$

where  $\kappa_{c \rightarrow vent}$  is the resistance of the flow from the capillary network to the ventricles via the amalgamated choroid plexuses.

Based on vascular wall-thickness arguments, there is no flow into or out of the arterial and venous blood networks, hence:

$$\begin{aligned} \frac{\partial}{\partial r} (p_a) &= 0 \quad \text{on } \Gamma_v \\ \frac{\partial}{\partial r} (p_v) &= 0 \quad \text{on } \Gamma_v \end{aligned} \quad (15a - b)$$

The blood pressures are given by arterial and venous blood pressures in Dirichlet form:

$$\begin{aligned} p_a &= p_{bpA} \quad \text{on } \Gamma_s \\ p_v &= p_{bp} \quad \text{on } \Gamma_s \end{aligned} \quad (16a - b)$$

It is assumed that there is no flow into or out of the arteriole/capillary blood network at the skull, negating the influence of any pial vessels:

$$\frac{\partial}{\partial r}(p_c) = 0 \text{ on } \Gamma_S \tag{17}$$

At the skull, CSF absorption causes a pressure difference dependent on the resistance to absorption via the arachnoid granulation,  $R$ , and the rate of CSF egress at the skull,  $Q_o$ :

$$p_e = p_v|_{\Gamma_S} + \mu^e R Q_o \text{ on } \Gamma_S \tag{18}$$

The increment of fluid content for each compartment,  $\zeta^A$ , in terms of volume dilation,  $\varepsilon_{VD}$  (see Eq. (20)) reads as:

$$\zeta_A = \alpha^A \left[ \varepsilon_{VD} + \frac{(1 - \alpha^A \beta) p^A}{K\beta} \right] \tag{19}$$

$\beta$  is defined as Skempton's coefficient (a measure of the distribution of the applied stress between the solid matrix and fluid). A value of  $\beta = 0.99$  (see Table 1) represents a saturated mixture where the applied load is nearly entirely supported by the CSF fluid.

Finally, the volume dilation ( $\varepsilon_{VD}$ ) is obtained from:

$$\varepsilon_{VD} = \varepsilon_r + \varepsilon_\theta = \frac{\partial u}{\partial r} + 2\frac{u}{r} \tag{20}$$

where  $\varepsilon_r$  is the radial strain, and  $\varepsilon_\theta$  is the tangential strain.

The final system (Eq. (9a–e) and boundary conditions) utilise a spherically symmetric geometrical representation. The parenchyma of an adult brain is represented as a spherical shell. The outer radius of this shell is given by  $r_M$ , whilst the lumped representation of the lateral ventricles is represented by another spherical shell with radius  $r_V$  (see Fig. 1b). Both radii are given in Table 1. The third and fourth ventricles along with the Sylvian aqueduct are assumed to be connected to the subarachnoid space (SAS).

The transient governing poroelastic equations are solved by utilising a second-order accurate central finite difference scheme on the inner nodes and the forward/backward Euler scheme on the boundary nodes for the spatial discretization. The Crank-Nicolson method is used for the temporal discretization. Initial conditions are also provided, which are:  $\mathbf{u} = \dot{\mathbf{u}} = 0$  and  $p_A = \bar{p}_A$ , where the latter represents the scalar pressures for each fluid compartment obtained from running the steady-state MPET simulation.

It is important to note the difference between the current model and previous work by the same authors. The quasi-steady model studied in previous work (Tully and Ventikos, 2011; Vardakis et al., 2013a) is identified from Eq. (9a–e) by considering only the terms within the square brackets, imposed by setting  $\partial/\partial t \rightarrow 0$ . All the additional terms (see Zienkiewicz et al., 1999) on the right hand side of the system equations that are taken into account in this work are clearly shown, in addition to the temporal variation in scalar pore pressure and fluid content due to local volume dilation ( $\nabla \cdot \mathbf{u}$ ) for each compartment. The core boundary conditions for the solid matrix displacement and pore pressure compartments have also been kept the same for simplicity.

2.5. Poroelastic constants

For the Young's modulus,  $E$ , the same value (584 Pa) as Taylor and Miller (2004) is used, since they treated brain parenchyma as a strain-rate dependent material, and is directed at hydrocephalus simulations. The section of brain that was used composed mainly of white matter, and the assumption made here is that both white and grey matter exhibit the same value of  $E$ .

A Poisson's ratio ( $\nu$ ) of 0.35 is adopted from Kaczmarek et al. (1997) and Taylor and Miller (2004), since this value conceptualises the relative compressibility of a biphasic mediums solid phase (in the fully drained configuration), and allows for fluid to be absorbed or relieved from the solid matrix (astrocytic water uptake mostly, for the four compartment MPET system). From the elastic modulus and Poisson's ratio, the remaining elastic moduli (for homogenous isotropic materials)

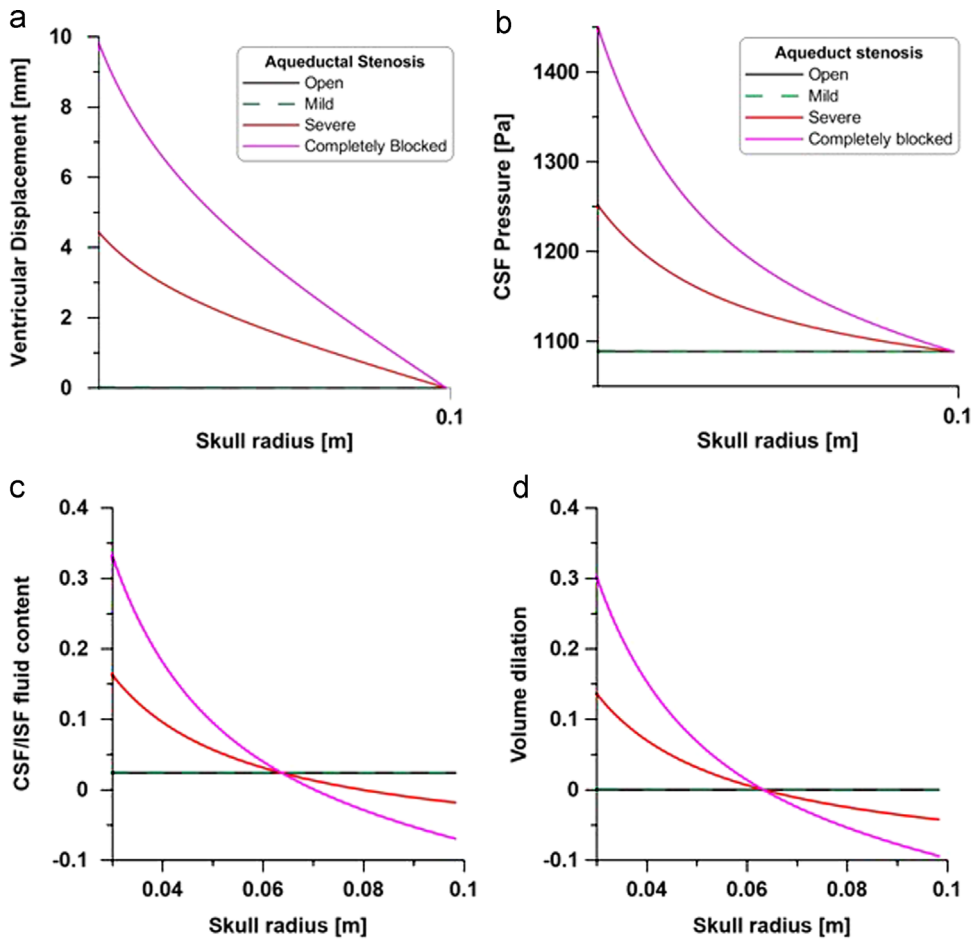


Fig. 2. Parenchymal displacement and CSF/ISF pore pressure. (a) Skull radius versus parenchymal displacement for the open aqueduct and its accompanying stenosed cases (mild, severe and completely blocked). The curves crossing the vertical axis imply the ventricular displacement. (b) Skull radius versus pore pressure for the CSF/ISF compartment at varying levels of aqueductal stenosis. The ventricular pressure is obtained by observing the points where the pressure curves cross the vertical axis. Both plots are taken after  $t = 86,400$  s (1 day). (c) Skull radius versus CSF/ISF fluid content after 1 day of simulation. (d) Skull radius versus the trace of the strain tensor (or volume dilation) after 1 day of simulation.

are obtained, namely the bulk modulus ( $K$ ), Lamé's first parameter ( $\lambda$ ) and shear modulus ( $G$ ). The values can be seen in Table 1. The same values as those in the pertinent literature are used, especially since it is known that observable differences between white and grey matter exist, however without concrete approval for a range of values from the scientific community. The pertinent literature all treats the parenchyma as a homogenous tissue for this reason (Tully and Ventikos, 2009, 2011; Smillie et al., 2005; Wirth and Sobey, 2006).

The poroelastic constants (Biot–Willis parameters, network transfer coefficients (Eq. (9a–e)), network permeabilities) are assumed to represent effectively saturated conditions, and are those used by Tully and Ventikos (2011), who performed a careful large scale parametric estimation study.

### 3. Results

From Fig. 2a and b it can be seen that both the parenchymal displacement and the radial CSF pressure are seemingly indistinguishable between the patent and mild cases of aqueductal stenosis, even though the diameter of the aqueduct has been reduced from 4 mm to 1 mm. The CSF pressure slightly increases from 1088.8 Pa to 1089.7 Pa between open aqueduct and mild stenosis. The ventricular displacement on the other hand shows an increase from approximately 0 mm to 0.03 mm. Considering the severe ( $d=0.25$  mm) and completely blocked ( $d=0$  mm) aqueduct, both CSF pressure and ventricular displacement show an increase from 1089.7 Pa and 0.03 mm in the mild case to 1251.4 Pa and 4.4 mm in the severely stenosed aqueduct, and finally 1449.0 Pa and approximately 1 cm in the completely blocked aqueduct.

Fig. 2c and d depicts the CSF/ISF fluid content and volume dilation respectively. The former is based on Eq. (19). The prior is obtained by Eq. (20), where both radial and tangential components of the strain are utilised. As can be seen, increasing stenosis with eventual atresia increases the level of CSF/ISF fluid content at the ventricles (at a skull radius of 3 cm) from 0.02 in the open case to 0.3 in the case for atresia. The volume dilation obeys similar trends, rising from a minute  $4 \times 10^{-6}$ , to 0.3 for the same cases. On the other end at the skull (skull radius of 10 cm), the fluid content and volume dilation pairs ( $\zeta$ ,  $\varepsilon_{VD}$ ) are  $(0.02, 4.5 \times 10^{-8})_{open}$  and  $(-0.07, -0.09)_{atresia}$ . The remaining pairs for mild and severe stenosis at the ventricles are:  $(0.025, 7.7 \times 10^{-4})_{mild}$  and  $(0.16, 0.14)_{severe}$ . At the skull, these are:  $(0.024, -2 \times 10^{-4})_{mild}$  and  $(-0.018, -0.042)_{severe}$ .

Fig. 3a shows the tracking of ventricular displacement over the simulation period of 24 h. As can be seen from the figure, an application of mild stenosis allows for a constant value of amalgamated ventricular displacement in under 0.1 days (2.4 h), whereas the application of a severe stenosis delays this settlement to approximately 10 h. Atresia (completely blocked aqueduct)

shows a clear sign of reaching a steady ventricular displacement after 24 h. Fig. 3b and c depicts the evolution of CSF pressure and parenchymal tissue displacement at five points in time ( $t=100$  s, 1 h, 3 h, 9 h and 24 h). CSF pressure at the ventricles increases from approximately 1095 Pa to 1251 Pa over this period. The parenchymal tissue displacement shows an increase in ventricular displacement (at a skull radius of 0.03 m), from approximately 50  $\mu$ m to 4.4 mm.

### 4. Discussion

The results in Figs. 2 and 3 show a strong qualitative correlation in the magnitude of ventricular displacement and CSF pressure. Similar results have been obtained by Tully and Ventikos (2009, 2011); Sobey and Wirth (2006); Smillie et al. (2005), where the predicted ventricular displacement approached 1 cm after 24 h of simulation time in SPET (single compartment poroelasticity), MPET and non-linear SPET cases which take into account a strain-dependent permeability. The degree of severe aqueductal stenosis between the simulations in this work and that of Tully and Ventikos (2011) match quite well, and the results here correlate favourably to the latter work, in both ventricular displacement (Figs. 2a and b, 3a) and CSF pressure (Fig. 3b). Therefore, the results in the present work first of all demonstrate that the quasi-steady hypothesis adopted in all the previously referenced works, including those involving the MPET formulation, is generally compatible with the solution of the fully transient system. That being said, we note that the quasi-steady approach slightly overestimates the degree of ventricular displacement and ventricular CSF pressure when compared with the fully transient system we address here, since the predicted results in this study required a completely blocked aqueduct to reach similar magnitudes in the aforementioned variables. The increased complexity in relaxing the quasi-steady constraint for the MPET system in both solid and liquid phases has not been considered before, and additionally, extends the notion of the mixed hyperbolic–parabolic classical Biot system, which is represented by considering the dynamic equilibrium equation for the poroelastic medium whilst extending the parabolic representation for the diffusive fluid flow (Showalter, 2000). Volume-distributed external forces are neglected in this MPET representation, and source densities are not volume distributed either (not a function of skull radius).

In line with previous studies (Sobey and Wirth, 2006; Smillie et al., 2005; Wirth and Sobey, 2009; Vardakis et al., 2013a), obtaining the fluid content in the CSF/ISF compartment (Fig. 2c) provides a

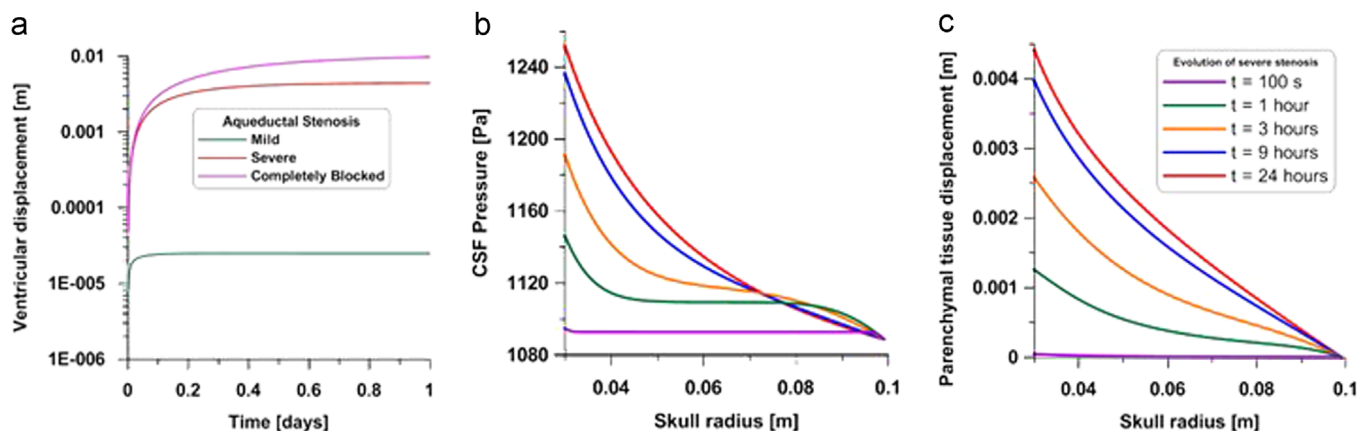


Fig. 3. Transient evolution of ventricular displacement and CSF pressure with time and skull radius. (a) Ventricular displacement is tracked with time for two degrees of stenosis severity (mild, severe) and atresia (completely blocked). (b) Transient evolution of CSF/ISF pore pressure within the parenchymal tissue. (c) Transient evolution of parenchymal tissue displacement between the ventricles and skull.

possible localised visualisation of periventricular tissue damage, as positive values of fluid content (swelling) are observed in these regions. The greater the degree of stenosis, the larger the dilation of parenchymal tissue near the ventricles. Near the skull, the trend is reversed, as the parenchymal tissue compresses near this region, and so more fluid is squeezed out of the tissue with increasing stenosis. This metric of comparison is mainly qualitative in nature, as physiologically relevant quantitative comparators are not available. Localised swelling in the periventricular region results in both stretch (adjacent to the ventricles) and compression (adjacent to the skull) of cortical tissue, as seen in Fig. 2d. Similar characteristics in the trace of the strain tensor are seen in analytical models of NPH (Shahim et al., 2012). Periventricular lucency (first witnessed by Naidich et al. (1976)) is represented by increased CSF/ISF content in the periventricular regions, and is assumed to result from ependymal surface breakdown which helps alleviate pressure in the ventricles by allowing for CSF extravasation (and oedema formation). It is speculated that this process could be achieved with the possible assistance of AQP4 (Papadopoulos and Verkman, 2013), which lines the ependymal surface.

Fig. 3b depicts the predicted evolution of the CSF pressure between 100 s and 1 day. It can be seen that through the use of the fully dynamic MPET model, important features of the results can be extracted. For instance, for the tissue region nearest to the skull (Skull radius  $> 0.07$  m), the family of CSF pressure curves show a relatively rapid increase in pressure between 100 s and 3 h. The increasing ventricular pressure (complemented with ventriculomegaly, see Fig. 3c) is causing the trans-parenchymal tissue region to respond, and this coping mechanism is most attenuated at the regions closest to the skull and the ventricles. After 9 h, the parenchymal tissue shows to be coping well with the additional pressure burden, since both ventriculomegaly and ventricular CSF pressure show small increases between 9 and 24 h (3.9–4.4 mm and 1236–1251 Pa respectively).

It is worth noting that experimental evidence (which is limited) exists of ventriculomegaly equilibrium in canine models of kaolin induced hydrocephalus (McCormick et al., 1992). Intraventricular pressure (IVP) rises to a peak value ( $\sim 6050 \pm 2700$  Pa) after  $\sim 24 \pm 12$  h, before it decreases to a steady value. This evolution is accompanied by gradual ventriculomegaly. In this work, more conservative estimates for IVP are observed in Fig. 3b, whilst ventricular enlargement stabilises after relatively short time frames. This is in many ways expected, since the parenchymal model being discussed possesses Biot–Willis parameters approximately equal to unity for all compartments. These theoretical values could minimise the influence of any possible compressible characteristics in the parenchyma, as it has been both shown and alluded to, that altering compartmental compliance (or inversely, elastance) plays a role in influencing ventriculomegaly in poroelasticity (Tully and Ventikos, 2011; Shahim et al., 2012; McCormick et al., 1992). In order to understand the full effects of such changes in the evolution of ventriculomegaly over long periods in time (of the order of days, weeks or years), it would be useful to observe any changes through the lens of communicating hydrocephalus, as opposed to the non-communicating case taken into account in this work. In this way, important factors such as out-flow resistance, parenchymal source/sink terms and small trans-parenchymal pressure gradients relating to the evolution of parenchymal tissue displacement can be analysed within the right context.

The limitations surrounding the proposed MPET model include the use of a linear stress–strain relationship in light of large strains. Altered pulsatility of the fluid compartments within the cerebral environment can also be investigated in more detail, as the fully dynamic MPET system has now been efficiently

discretised. Extending the discretization to three dimensions in addition to relaxing the spherically symmetric assumption will also allow one to fully capture the order of dilation of the four cerebral ventricles. In future work, the theoretical values of compliance ( $\alpha^{a,c,v}$ ) of the three blood compartments (arterial, capillary and venous blood) will be investigated to see how disease progression allied to communicating and obstructive hydrocephalus effects the pressure profiles of different compartments in addition to the parenchymal tissue displacement.

It was mentioned earlier in the manuscript (§2.5) that observable differences between white and grey matter exist, however consistent values have not been reported in the literature, hence the assumption of homogeneous parenchymal tissue. Magnetic Resonance Elastography (MRE) is an accurate and non-invasive technique that is used to provide mechanical properties (shear stiffness) of the human brain in vivo (Weaver et al., 2012; Schregel et al., 2012). Although studies in this field look promising, consistent and agreeable values are not yet established (Sack et al., 2008; Kruse et al., 2008). The use of diffusion tensor imaging (DTI) also allows for the investigation of brain matter microstructure in a non-invasive manner. White matter fibres for example can be juxtaposed with the storage moduli obtained from MRE in order to observe the more intricate spatial variation in mechanical properties (Johnson et al., 2013), and thus introduce anisotropy in the MPET model. Relaxing the constraint of isotropic permeability of the fluid networks can also allow further exploration of diminishing blood flow.

It is important to consider that although the focus of this manuscript is on the influence of aqueductal stenosis utilising, for the first time, the full transient form of the governing equations, the fully dynamic MPET system can be implemented in a much broader setting. In this MPET model, the boundary conditions are based on the classical hypothesis of CSF transport. The extension to the more intricate understanding of the recently discovered glymphatic pathway (Iliff et al., 2012) is currently being developed though the addition of compartments in order to better mimic parenchymal tissue. Astroglial water pressure–flux relationships are also being developed in collaboration with experiments, as a means of informing this extended MPET model. The aim is to be able to model more recent hypotheses surrounding CSF transport (which includes newly discovered central nervous system lymphatic vessels (Aspelund et al., 2015; Louveau et al., 2015)).

## 5. Conclusions

We have presented a set of fully dynamic, four-network poroelastic simulations that take into account artificially imposed aqueductal stenosis (mild and severe) and complete blockage (atresia) of the Sylvian aqueduct. Swelling can be observed in the form of positive values of CSF/ISF fluid content near the ependyma, whilst CSF/ISF drainage appears to act near the skull (negative values of CSF/ISF content). Cortical stretching (positive values of volume dilation) and compression (negative values of volume dilation) is observed in the regions close to the ventricles and skull, respectively. Finally, interesting pressure and displacement profiles can be observed in relation to the parenchymal tissue coping mechanism over a period of 24 h, whereby the ability of the parenchyma to withstand the additional pressure burden (observed via the gradual increase in ventriculomegaly and CSF/ISF pressure, after 9 h of simulation) as a function of stenosis severity seems to be most pronounced in tissue around the vicinity of the skull and ventricles.

## Conflict of interest statement

We wish to confirm that there are no known conflicts of interest associated with this publication and there has been no significant financial support for this work that could have influenced its outcome.

## Acknowledgements

We acknowledge support, contributions and insight from VPH-DARE@IT (FP7-ICT-2011-9-601055), a collaborative Research Project funded under the Co-operation specific programme of the Seventh Framework Programme of the European Union for research, technological development and demonstration activities.

## References

- Aspelund, A., Antila, S., Proulx, S.T., Karlsen, T.V., Karaman, S., Detmar, M., Wiig, H., Alitalo, K., 2015. A dural lymphatic vascular system that drains brain interstitial fluid and macromolecules. *J. Exp. Med.* 212 (7), 991–999.
- Biot, M.A., 1941. General theory of three-dimensional consolidation. *J. Appl. Phys.* 12, 155–164.
- Bruni, J.E., 1998. Ependymal development, proliferation and functions: a review. *Microsc. Res. Tech.* 41, 2–13.
- Cinalli, G., Spennato, P., Aliberti, F., Cianciulli, E., 2010. Aqueductal stenosis. In: Mallucci, C., Sgouros, S. (Eds.), *Cerebrospinal Fluid Disorders*. Informa Healthcare USA, Inc, New York, pp. 154–188.
- Corns, R., Martin, A., 2012. Hydrocephalus. *Neurosurgery* 30, 142–148.
- Iloff, J.J., Wang, M., Liao, Y., Plogg, B.A., Peng, W., et al., 2012. A paravascular pathway facilitates CSF flow through the brain parenchyma and the clearance of interstitial solutes, including amyloid  $\beta$ . *Sci. Transl. Med.* 4, 1–11.
- Jellinger, G., 1986. Anatomopathology of non-tumoral aqueductal stenosis. *J. Neurosurg. Sci.* 1, 1–16.
- Johnson, C.L., McGarry, M.D.J., Gharibans, A.A., Weaver, J.B., Paulsen, K.D., et al., 2013. Local mechanical properties of white matter structures in the human brain. *NeuroImage* 79, 145–152.
- Kaczmarek, M., Subramaniam, R., Neff, S., 1997. The hydromechanics of hydrocephalus: steady-state solutions for cylindrical geometry. *Bull. Math. Biol.* 59, 295–323.
- Kruse, S.A., Rose, G.H., Glaser, K.J., Manduca, A., Felmlee, J.P., Jack, C.R., Ehman, R.L., 2008. Magnetic Resonance Elastography of the brain. *NeuroImage* 39, 231–237.
- Levine, D.N., 1999. The Pathogenesis of Normal Pressure Hydrocephalus: A Theoretical Analysis. *Bull. Math. Biol.* 61, 875–916.
- Levine, D.N., 2000. Ventricular size in pseudotumor cerebri and the theory of impaired CSF absorption. *J. Neurolog. Sci.* 177 (2), 85–94.
- Louveau, A., Smirnov, I., Keyes, T.J., Eccles, J.D., Rouhani, S.J., Peske, J.D., Derecki, N.C., Castle, D., Mandell, J.W., Lee, K.S., Harris, T.H., Kipnis, J., et al., 2015. Structural and functional features of central nervous system lymphatic vessels. *Nature* 523 (7560), 337–341.
- McCormick, J.M., Yamada, K., Rekte, H.L., Miyake, H., 1992. Time course of intraventricular pressure change in a canine model of hydrocephalus: its relationship to sagittal sinus elastance. *Pediatr. Neurosurg.* 18 (3), 127–133.
- Naidich, T.P., Epstein, F., Lin, J.P., Kricheff, I.L., Hochwald, G.M., 1976. Evaluation of pediatric hydrocephalus by computed tomography. *Radiology* 119 (2), 337–345.
- Papadopoulos, M.C., Verkman, A.S., 2013. Aquaporin water channels in the nervous system. *Nat. Rev. Neurosci.* 14 (4), 265–277.
- Rekte, H.L., 2009. A contemporary definition and classification of hydrocephalus. *Semin. Pediatr. Neurol.* 16, 9–15.
- Rice, J.R., Cleary, M.P., 1976. Some basic stress diffusion solutions for fluid-saturated elastic porous media with compressible constituents. *Rev. Geophys.* 14, 227–241.
- Russel, D., 1949. Observations on the Pathology of Hydrocephalus (Medical Research Council, Special Report Series). 265. His Majesty's Stationary Office, London.
- Sack, I., Beierbach, B., Hamhaber, U., Klatt, D., Braun, J., 2008. Non-invasive measurement of brain viscoelasticity using magnetic resonance elastography. *NMR Biomed.* 21, 265–271.
- Schregel, K., Wuerfel, E., Garteiser, P., Gemeinhardt, I., Prozorovski, T., Aktas, O., Merz, H., Petersen, D., Wuerfel, J., Sinkus, R., 2012. Demyelination reduces brain parenchymal stiffness quantified in vivo by magnetic resonance elastography. *Proc. Natl. Acad. Sci. USA* 109 (17), 6650–6655.
- Shahim, K., Drezet, J.M., Martin, B.A., Momjian, S., 2012. Ventricle equilibrium position in healthy and normal pressure hydrocephalus brains using an analytical model. *J. Biomech. Eng.* 134 (4), 041007.
- Showalter, R.E., 2000. Diffusion in poro-elastic media. *J. Math. Anal. Appl.* 251, 310–340.
- Smillie, A., Sobey, I., Molnar, Z., 2005. A hydroelastic model of hydrocephalus. *J. Fluid Mech.* 539, 417–443.
- Sobey, I., Wirth, B., 2006. Effect of non-linear permeability in a spherically symmetric model of hydrocephalus. *Math. Med. Biol.* 23, 339–361.
- Spennato, P., Tazi, S., Bekaert, O., Cinalli, G., Decq, P., 2013. Endoscopic Third Ventriculostomy for Idiopathic Aqueductal Stenosis. *World Neurosurgery* 79 (2, Suppl), S21.e13–S21.e20.
- Stagno, V., Navarrete, E.A., Mirone, G., Esposito, F., 2013. Management of hydrocephalus around the world. *World Neurosurg* 79 (2 Suppl), S23.e17–20.
- Taylor, Z., Miller, K., 2004. Reassessment of brain elasticity for analysis of biomechanisms of hydrocephalus. *J. Biomech.* 37, 1263–1269.
- Thompson, D., 2009. Hydrocephalus. *Neurosurgery* 27, 130–134.
- Tully, B., Ventikos, Y., 2009. Coupling poroelasticity and CFD for cerebrospinal fluid hydrodynamics. *IEEE Trans. Biomed. Eng.* 56, 1644–1651.
- Tully, B., Ventikos, Y., 2011. Cerebral water transport using multiple-network poroelastic theory: application to normal pressure hydrocephalus. *J. Fluid Mech.* 667, 188–215.
- Vardakis, J.C., Tully, B.J., Ventikos, Y., 2013a. Multicompartmental poroelasticity as a platform for the integrative modeling of water transport in the brain. In: Holzapfel, E., Kuhl, E. (Eds.), *Computer Models in Biomechanics*. Springer, Netherlands, pp. 305–316.
- Vardakis, J.C., Tully, B.J., Ventikos, Y., 2013b. Exploring the Efficacy of Endoscopic Ventriculostomy for Hydrocephalus Treatment via a Multicompartmental Poroelastic Model of CSF Transport: A Computational Perspective. *PLoS ONE* 8 (12), 84577, 2013b.
- Weaver, J.B., Pattison, A.J., McGarry, M.D., Perreard, I.M., Swienkowski, J.G., Eskey, C.J., Lollis, S.S., Paulsen, K.D., 2012. Brain mechanical property measurement using MRE with intrinsic activation. *Phys. Med. Biol.* 57, 7275–7287.
- Wirth, B., Sobey, I., 2006. An axisymmetric and fully 3D poroelastic model for the evolution of hydrocephalus. *Math. Med. Biol.* 23, 1–26.
- Wirth, B., Sobey, I., 2009. Analytical solution during an infusion test of the linear unsteady poroelastic equations in a spherically symmetric model of the brain. *Math. Med. Biol.* 26, 25–61.
- Zienkiewicz, O.C., Chan, A.H.C., Pastor, M., Schrefler, B.A., Shiomi, T., 1999. *Computational Geomechanics with Special Reference to Earthquake Engineering*. John Wiley & Sons Ltd., England, UK.